

Finite life fatigue design of spiral springs of dual-mass flywheels: Analytical estimation and experimental results

Daniela Maffiodo¹, Raffaella Sesana¹ , Dino Paolucci² and Sabrina Bertaggia²

Abstract

A procedure to design the spiral springs finite life for dual-mass flywheels is presented. Due to design constraints, installation space, production processes, stiffness requirement, maximum torque, and maximum speed, these components are dimensioned for finite life. Two- and three-dimensional finite element model static structural analysis was performed to obtain the stress distribution, deformed shape, and to validate optimization design. The fatigue analysis was performed both experimentally and by means of a component life estimation model. An experimental duty cycle was applied. Finite element analysis and experimental analysis agree in pointing out the location and the value of maximum stresses and the shape of deformation. Vehicle tests highlight premature spiral springs' failures, which do not agree with life estimation. The examination of the fracture showed that fretting and wear, along with fatigue phenomena, are the causes of premature failures. A dedicated component life estimation model is required, taking into account of wear and loading history.

Keywords

Finite element model, dual-mass flywheel, fatigue, failure, spring, life estimation

Date received: 30 December 2017; accepted: 13 April 2018

Handling Editor: Shun-Peng Zhu

Introduction

Automotive powertrains with piston engines generate a time-dependent torque, which mainly depends on engine speed and number of cylinders. This variable torque introduces annoying vibrations, which affect the whole system. Such an issue is especially critical since the need to find a compromise between increasing engine efficiency, due to current CO₂ reduction laws, and maintaining engine performance can introduce increased torsional vibrations in the drive train of future engines.

The scenario in which design engineers currently operate is rather challenging. On one hand, performance requirements in terms of vibrations dampening and filtration are becoming more and more strict. On

the other hand, latest engine design aims at power increase and cross section reduction of crankshaft and gearbox shaft, with the consequent increase in crankshaft oscillations transmitted to the gearbox.

Crankshaft and other mechanical parts of the engine are designed to dampen high-frequency oscillations in

¹Dipartimento di Ingegneria Meccanica e Aerospaziale (DIMEAS), Politecnico di Torino, Torino, Italy

²Dayco, Ivrea, Italy

Corresponding author:

Raffaella Sesana, Dipartimento di Ingegneria Meccanica e Aerospaziale (DIMEAS), Politecnico di Torino, Corso Duca degli Abruzzi, 24, 10129 Torino, Italy.

Email: raffaella.sesana@polito.it



the engine torque, so low-frequency oscillations at low engine speeds have to be dampened by additional devices. This has been done for a long time by means of conventional flywheels attached to the crankshafts, which also have the effect of regularizing. As a high inertia is needed to achieve required dampening at low engine speeds, this causes delays on the engine response to input changes. For this reason, solid flywheels are not suitable for demanding applications such as mid-range, luxury class, and sport cars.

To cope with these problems, the dual-mass flywheel (DMF) was introduced. In these devices, inertia is split into two parts: the primary mass is connected to the crankshaft, while the secondary mass is part of the clutch. Common DMF design, currently used by several manufacturers, has two stoppers constraining the coil springs (usually arc-shaped) which are the actual filtering elements. As the arc springs deflect within the arc channel, they transfer torque from the primary mass to the secondary mass. When the arc springs slide through their channel, friction adds dampening characteristics to the device.^{1,2}

This device increases the functionality of the gearbox, its durability, and driver comfort. Theodossiades et al.³ demonstrated with an experimental comparative study that the use of DMF reduces noise with respect to the solid flywheel.

Furthermore, adoption of such a solution can result in a significant fuel savings when compared to systems with rigid flywheels.⁴ All these reasons justify the high increase in the number of vehicles fitted with a DMF during the last 15 years. Moreover, the share of vehicles in Europe equipped with a DMF is estimated to increase to about 40% by 2018.

DMF equipped with coil springs presents some disadvantages due to their geometry and operating conditions.^{5,6} Friction between arc-shaped coil springs and external surface track may cause an undesired behavior: the transmitted torque as a function of angular displacement presents a hysteresis loop, wider at high speeds, due to forces acting radially on the springs.⁷ In addition, different angular displacements between coast and drive conditions may occur. Moreover, stiffness and damping change dramatically when engine speed increases: due to the friction, the number of active coil springs is reduced, thus leading to an increase in the actual spring stiffness and to a reduction in the filtering capacity. Last but not least, although sealing should be guaranteed by welding, grease leakage represents the main failure modes for this device.

With the aim of improving the device performance, various researchers are working on the modeling of the system^{8,9} and on the experimental characterization of its behavior.¹⁰ Kang et al.¹¹ measured the angular displacement between the primary flywheel mass and the

secondary flywheel mass of a DMF by installing a linear variable differential transformer (LVDT)-based sensor in a real manual transmission vehicle. Using a temperature sensor, they also evaluated transmitted torque. Chen et al.⁷ experimentally studied stiffness nonlinearity of DMFs and the hysteretic behavior of frictional torque, thereby building a nonlinear 2-degree-of-freedom model.

To reduce drawbacks due to friction, some researchers introduced pads between the springs and the external channel. Damper concepts which allow good isolation at low speeds are also under investigation. Adopted approaches include the introduction of a secondary inner damper in series or the use of a centrifugal pendulum absorber. Generally speaking, these proposals lead to more complex design due to the adding of new parts.

A possible alternative solution, which was recently patented,^{12–14} consists in the use of a DMF in which the filter system is composed of spiral springs which replace the classical arc coil springs. The device can be employed both for manual gearboxes and for hybrid automatic transmissions. Its distinctive feature is that the elastic behavior is defined almost exclusively by the stiffness of spiral springs, being marginally affected by torque and rotational speed. Moreover, the system does not require any lubrication, so there is no need for a seal closing.

The aim of this work is to investigate on critical points affecting finite life fatigue design of spiral springs in a commercially available DMF.

Figure 1(a) displays an exploded view of the analyzed DMF. The main parts are the primary flywheel (1) with or without retainers (2), the filtering device (3), the idling device (4), the start-up device (5), and the secondary flywheel (6).

Figure 1(b) shows a view of the investigated DMF, with two spiral springs (*s*), inner springs holder (*ir*) and outer spring holders (*or*), and a hard stop in the middle (*hs*), which prevents angular displacements over the imposed limit.

Retainers (see 2, Figure 1) can be added in order to limit the excessive enlargement of outer coils during operation: they are plastic components, placed in the outer space between spring and carter. Design of these elements is based on the shape of the deformed spring in a defined loading case.

Figure 2 shows the static characteristic (torque versus angular displacement) of the filtering device obtained by means of a quasi-static test. The dynamic characteristic has a trend independent from rotational speed since no significant friction is originated by centrifugal force. The drive condition (engaging) is represented in the left part of the diagram, that is, for negative angular displacement. In this condition, the

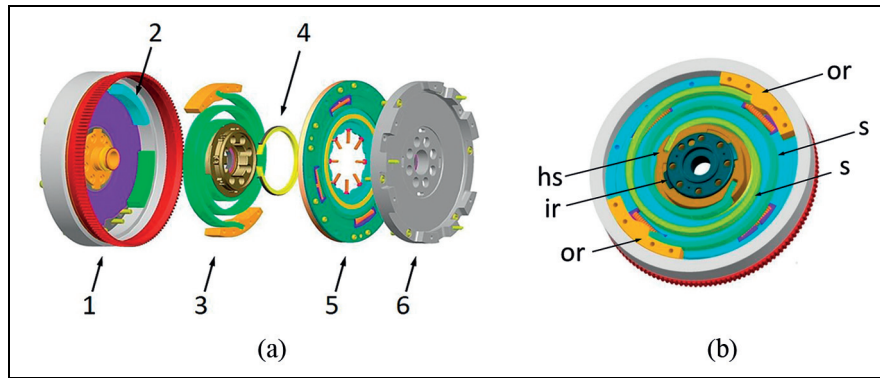


Figure 1. (a) Displays an exploded view of the analyzed DMF. The main parts are the primary flywheel (1) with or without retainers (2), the filtering device (3), the idling device (4), the start-up device (5), and the secondary flywheel (6). (b) Detail of the DMF.

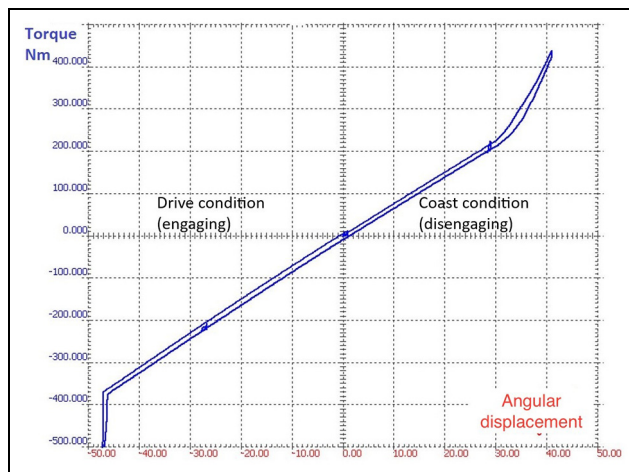


Figure 2. Filtering device with spiral springs—static characteristic (torque vs angular displacement; Dayco—all rights reserved).

springs are compressed and maintain stiffness constant until the maximum angular displacement corresponding to hard stop activation. This is a condition normally characterized by high torque. The hysteric cycle is mainly due to friction occurring between the springs and the side pads, which help maintaining the springs on the set plane and reducing noise. The coast condition (disengaging) is described in the right part of the diagram, that is, for positive angular displacement. In this case, the springs unroll maintaining stiffness constant until they come in contact with the retainers, which are parts that limit the springs' centrifugal expansion.

The global system has a good performance behavior in terms of filtering and vibration cutting. Nevertheless, the springs' fatigue life represents its weak point, due to the high stresses which occur in the most severe working conditions.

This article describes the algorithm and procedures which have been used to define the spiral springs finite life design for the considered DMF design guidelines are proposed in order to focus on the aspects which are directly connected to fatigue analysis and verification of target life.

Materials and method

Analysis procedure

The employed procedure, based on finite element analysis (FEA), is adequate for the design of automotive components which present many critical issues such as large displacements, unusual material constitutive model, variable amplitude fatigue loading, dynamic effects, and geometrical complexities (e.g. contacts and notches). It can be used for the minimization of testing activities and in the specific case of flywheel. In particular, the procedure integrates the results coming from static FEA simulations (in loading conditions given by the load counting methods after the actual duty cycle), load counting methods (which provide the equivalent loads applied to the component after the duty cycle) and life calculation methods, which take into account several critical failure causes.

The design procedure is split in two steps: static analysis and fatigue analysis. Static analysis aims at obtaining an effective FEM to estimate stresses in the coils for the different (static) loading conditions of the component. A reduced experimental validation is performed to validate and optimize the model. Fatigue analysis aims at estimating the life of the component when a duty cycle is applied in variable amplitude loading conditions. This analysis matches the stress estimation from static structural analysis with a stress counting method derived from experimental acquisitions (duty cycle) and with a life estimation model. Experimental validation leads to an assessment of the effectiveness of the whole procedure.

Static analysis

Static analysis, articulated in four steps, aims at validating the FEMs by means of static structural analyses, the results of which are compared with analytical and experimental results.

The first step consists in the analytical calculation of stresses in coil springs caused by static torque and centrifugal forces (with no retainers, see Figure 1). The analytical calculation assumes the spring to behave as a cantilever coil beam with a rectangular cross section and Archimedes spiral axis undergoing bending. Such a scheme neglects energy dissipation and does not consider the tensile force, which is actually present during the DMF operation. While the DMF is subjected to loading, the springs bend in the imaginary plane that contains Archimedes spiral axis, thus allowing a relative rotation between the internal and external spring holders.

According to this model, bending moment due to engine torque is constant along the whole spring length, so the maximum stress is computed, given the rotation associated with a defined engine torque M_o , with the following equation

$$\sigma_{max} = \frac{M_o}{W_b} \quad (1)$$

where M_o is the torque applied on a single coil spring due to engine action and W_b is the cross-sectional bending modulus. The second step of the procedure consists in the implementation of a two-dimensional (2D) finite element model (FEM) of the spring, which identifies worst loading conditions in terms of stresses and displacements (with no retainers). Furthermore, these models aim at calculating the maximum stresses and their locations for the different loading configurations. Obtained results are thereafter compared to analytical ones (from first step) to verify model reliability. The stress field along the springs is assumed to be planar. According to De Saint Venant's hypotheses, this assumption is valid if the spring position, in which the stresses are calculated, is not close to neither the internal nor the external hooks. That is why a further three-dimensional (3D) FEM analysis is required to investigate the stress distribution corresponding to the inner hook connection point.

Several simulations are run by combining different torque-speed conditions. Stresses and strains in the coils are calculated in these conditions for DMF with and without retainers.

By considering the worst overspeed condition, the third step follows: choice of the retainers' optimal design is based on the analysis of the configuration which corresponds to the lowest maximum stress, that is, in coast conditions, close to the inner hook connection point.

The procedure is concluded by carrying out an experimental validation of simulation results by means of a test rig in which flywheels with retainers are subjected to four loading conditions (maximum positive and negative torque, in static and at maximum speed conditions) (fourth step). Strain data, measured on the flywheels in eight defined points equipped with strain gauges, are then compared to simulation results.

Fatigue analysis

Fatigue resistance of automotive components may be influenced by many factors such as stress concentrations due to specimen geometry, material inhomogeneity, presence of defects, and environmental actions. In the case of variable amplitude loadings, which are typical of irregular loads applied to real components during service conditions, definition of the number of cycles leading to fatigue failure is a non-trivial task. The approach commonly adopted is to convert the loading history into a set of fatigue cycles using a cycle counting method and then to compute total damage produced by the load by summing the damage produced by each counted cycle.^{15,16} Counting methods and damage accumulation rules allow calculation of total damage as a function of damage increments associated with each counted cycle.

The Palmgren-Miner linear damage rule¹⁷ is often adopted for its simplicity and efficiency. This model relates fatigue damage accumulation to the work absorbed by the material during cycle repetitions in a constant amplitude test. Failure occurs when total absorbed work reaches a critical level, which may vary between 0.5 and 2. The linear rule is simple but is load-level and load-sequence independent, and it neglects cycle interaction effects, often observed in experiments which produce crack growth acceleration and/or retardation. Other algorithms such as the "pagoda-roof method"¹⁸ and the "tank method" can also be employed.

The Rainflow method¹⁸ is the most popular and used counting procedure, since it has been recognized as the most accurate in identifying damaging events in case of complex loadings.^{19,20} In the literature, there are several different algorithms defining the Rainflow method, based on different rules, which however lead to the same results. The method does not consider the exact time history of each cycle, so the resulting computation cannot take into account any retardation or acceleration effect. Other counting methods are available in the literature, but the results, which derive from their application, do not lead to appreciable differences.²¹

In this research, fatigue analysis was performed in three steps. The first step consisted in the experimental fatigue characterization of the component. The spring was fatigue tested on a laboratory test rig, and the $S-N$

Table 1. FEA materials properties.

Application	Material	Yield stress (MPa)	UTS (MPa)	ν (–)	E (MPa)	E_t (MPa)
Spiral springs	54SiCrV6	1661	1795	0.3	206,000	4847
Spring holder	39NiCrMo3	685	880	0.3	206,000	1700
Retainers	Polyamides PA46	48	58	0.3	1000	–

FEA: finite element analysis; UTS: ultimate tensile strength.

diagram (where the stress is obtained by strain measurements in the most stressed point in the spring) was obtained. This diagram was subsequently used to estimate the endurance of the component in the damage model defined in the following step.

The second step consisted in the definition of a suitable duty cycle for the specific DMF application, of a proper cycle counting method, and of an adequate damage model. Based on these choices, endurance in duty cycle conditions can be estimated using stress values obtained from 2D and 3D model simulations. In particular, 2D simulations pointed out the worst working conditions and the related most stressed points. Then, a deeper 3D static structural analysis allowed obtaining a better evaluation of 3D stress distribution in the most stressed points for each considered loading condition. These values were the input data for the fatigue counting routine. Other inputs for the damage model came from experimental testing on material mechanical properties and component fatigue behavior (*S-N* curve).

A dedicated routine which combines the Rainflow counting method¹⁸ and Miner's damage rule was implemented in MATLAB environment.

For what concerns the duty cycle, the fatigue life estimation considers the sum of events occurring to the DMF per km, that is, the number of gear shifts, accelerations, and decelerations; in other terms, the number of events is the number of load changes.

A duty cycle is a mix of driving configuration, composed by city, highway, mountain, and sport driving mode. Each phase is characterized by a time percentage, which refers to the total driving time. In order to face a fatigue computation, it is necessary to evaluate the frequency of events, which describes a single stress cycle. This is obtained by means of experimental run out to acquire time, throttle pedal position, and engine speed data in several defined driving conditions (city, highway, downhill, sport, etc.)

Then, driving configuration data (time, throttle pedal position, and engine speed) are correlated to engine torque, by means of laboratory tests with an instrumented engine, working in discrete driving configurations, corresponding to the duty cycle ones.

Then, the engine torque data are correlated with stresses values on the spring, in all driving

configurations, by means of FEM simulations. That is, FEM simulations, running given a torque value, return the stresses in the spring.

This way, the load driving duty cycle can be converted in stress duty cycle, and fatigue counting methods and damage calculation can lead to endurance estimation of the component in duty cycle conditions.

Finally, in the third step of analysis, road tests were performed to compare fatigue endurance estimation results to the actual performance of the considered DMF. In the literature, other papers present similar procedures,^{20,22} but only few report the results of experimental validation.

FEMs

In order to understand the mechanical problem, a simplified 2D FEM was developed describing the main device characteristics, that is, the spring behavior as a function of speed rotation and torque, the deformed shape in order to verify contacts between coils, and the stress distribution along the coil.

The springs' material and the spring holders material are modeled as bilinear plastic characteristic, while the retainers are modeled with a linear elastic characteristic (Table 1). Table 1 data are obtained by supplier data-sheets (54SiCrV6 and PA 46) and from Standard UNI EN 10089:2006 (39NiCrMo3).

Simulations were performed by means of ANSYS 15.0.

In Figure 3, the 2D mesh is presented. The mesh elements are PLANE183, quadrilateral with eight nodes, the thickness is defined by a real constant. This element has a quadratic displacement behavior and is well suited to modeling irregular meshes. It is defined by eight nodes having two degrees of freedom at each node. It can be used as a plane element (plane stress, plane strain, and generalized plane strain). The contact is defined with a target line (stiffer element) and a contact line (less stiffer element: spring). A friction coefficient (0.15) and a penetration tolerance are defined.

A 3D model, SOLID187, was then implemented to analyze the 3D stress status in the most stresses areas in working conditions and where failure occurred, that is, corresponding to the inner hook position (Figure 4). The used element SOLID 187 has a quadratic

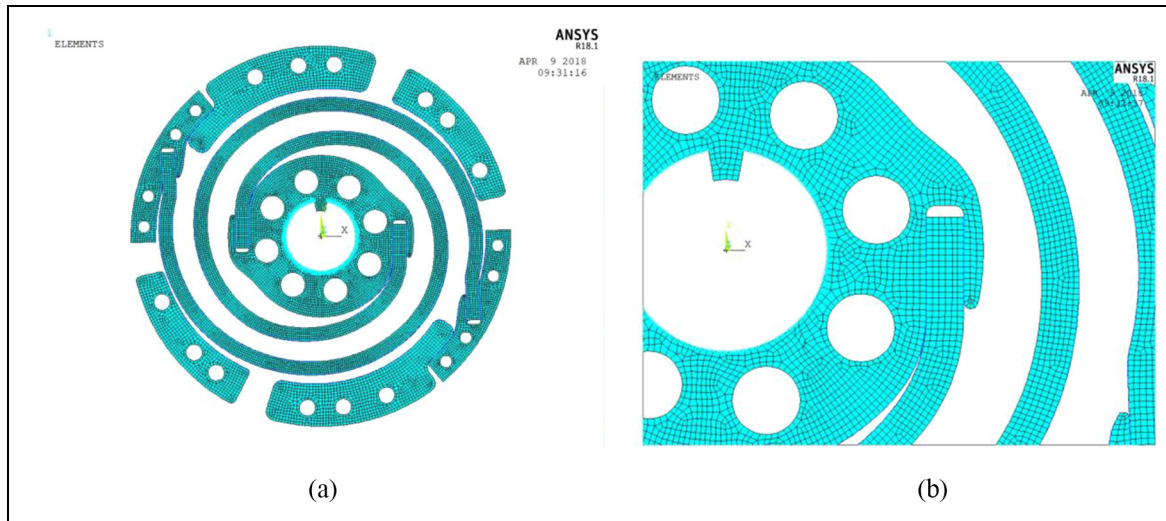


Figure 3. 2D FEA model with mesh (left) and detail (right).

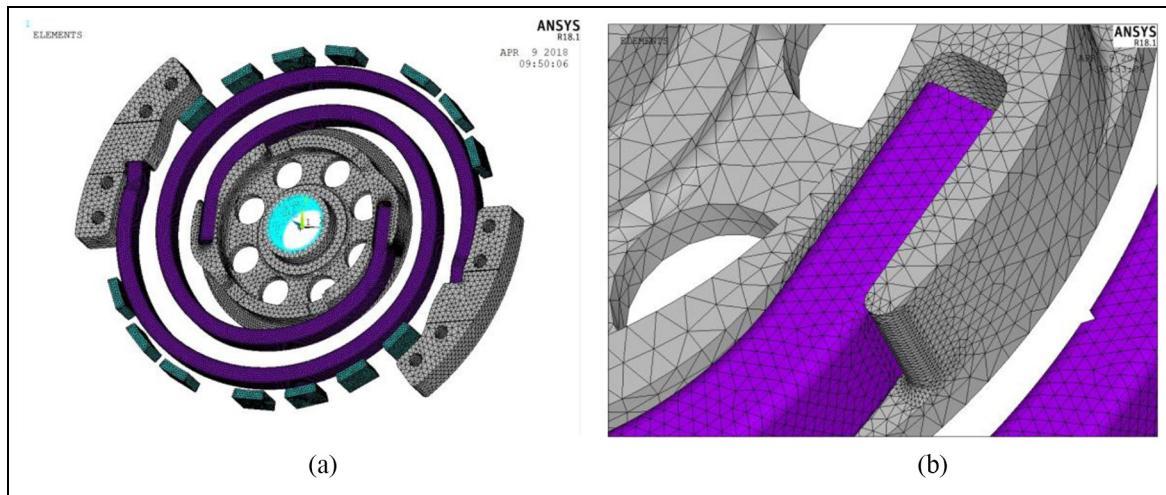


Figure 4. 3D FEA model with mesh (left) and detail (right).

displacement behavior and is well suited to modeling irregular meshes. This element is defined by 10 nodes having three degrees of freedom at each node. The contact is defined with a target surface (stiffer element) and a contact surface (less stiffer element: spring). A friction coefficient (0.15) and a penetration tolerance are defined.

Results and discussion

FEA simulation results

Results of analytical and numerical computations are reported in Table 2.

The 2D simulations pointed out that the critical load cases are two types: the first one is characterized by maximum torque and null rotational speed (Drive, i.e.

positive torque, and Coast, i.e. negative torque and conditions) and the second case is characterized by maximum rotational speed and a low negative torque (centrifugal).

Coast condition does not represent a possible working configuration; however, it is useful to verify that no plastic deformations are reached, moreover this condition corresponds with the deformation in case of very-high rotation speeds.

Simulation of springs at maximum rotational speed (6000 rpm) show large deformations and stresses and dangerous contacting surfaces. These results are validated by means of experimental testing. To avoid these problems, retainers were designed (see Figure 1).

Other simulations of the device without retainers were run at lower rotational speeds and the results are

Table 2. Stress calculation results.

	Loading condition	σ_{max} (MPa) Analytic model	σ_{max} (MPa) 2D FEM	Location ^a
Static (no retainers)	Maximum drive	1111	1377	at 180°
	420 Nm, 0 rpm	662	623	at 180°
	Coast -250 Nm, 0 rpm		896	at 120° (maximum value)
Centrifugal (no retainers)	6000 rpm, -40 Nm	—	1790	at 180°
	1400 rpm, 350 Nm	—	1050	at 180°
	4000 rpm, 350 Nm	—	1181	at 10°
Static (with retainers)	Coast -250 Nm, 0 rpm		796	at 10°
Centrifugal (with retainers)	6000 rpm, -40 Nm		1103	at 10°

2D: two-dimensional; FEM: finite element model.

^aangle measured from inner spring holder.

reported in Table 2. The same conditions were simulated on the device with retainers, and the results are reported in the same table, showing the decrease in stress distribution obtained by means of retainers in all the considered loading conditions.

For spring in maximum drive conditions, the FEA shows that the coil maximum stress σ_{max} is about 20% higher than the analytical one computed with the analytical formula. The main reason of this difference is due to the fact that the analytic model neglects the tensile force on the springs, indeed it considers only a pure torque.

Generally speaking, it resulted that analytic calculation underestimates the stresses as it neglects the axial component of the load.

Experimental validation of FEM simulations

Some springs were equipped with strain gauges, which positions are shown in Figure 5. In Figure 6(a), the experimental test rig is presented. Springs were

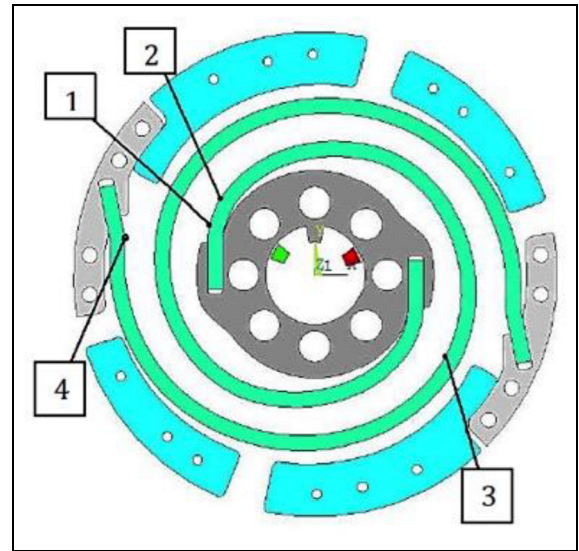
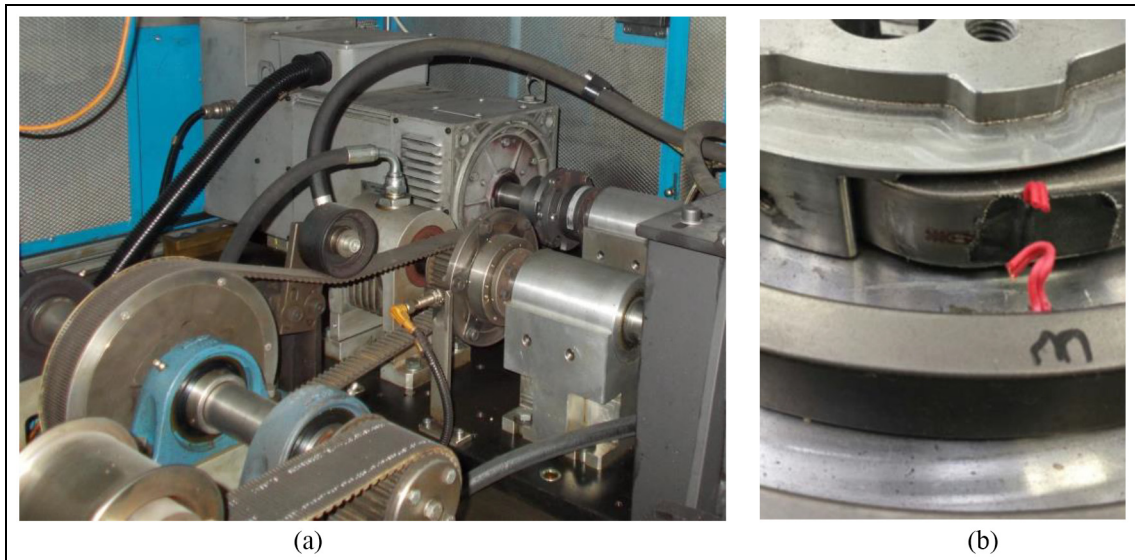
**Figure 5.** Strain gauges location for experimental testing.**Figure 6.** (a) Static testing rig and (b) example of strain gauge positioning.

Table 3. Simulated versus experimental stresses in different loading conditions.

Strain gauge	Torque −40 Nm			
	0 rpm		6000 rpm	
	Simulated stress (MPa)	Experimental stress (MPa)	Simulated stress (MPa)	Experimental stress (MPa)
1	−145	−128	−930	−795
2	−150	−141	−860	−821
3	148	145	802	775
4	141	129	690	638

Strain gauge	Torque +250 Nm			
	0 rpm		6000 rpm	
	Simulated stress (MPa)	Experimental stress (MPa)	Simulated stress (MPa)	Experimental stress (MPa)
1	756	697	92	28
2	817	768	−202	−192
3	−985	−978	430	428
4	−650	−633	653	641

equipped with strain gauges (Kiowa KFG-1-120-C1-11L1M2R, gauge length of 1 mm, 120 Ohm) positioned in a set of points indicated by 2D FEM analysis. Strain gauges measuring direction was parallel to the spring beam axis (principal direction). Rotating contact was obtained by means of slip rings. An example of strain gauge positioning is reported in Figure 6(b). These springs were tested in simulation conditions, and the measured strains multiplied by the elastic modulus gave the experimental stresses which were then compared with simulated ones.

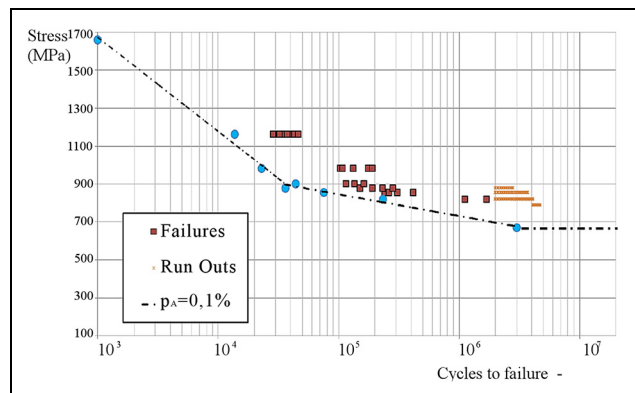
The results are reported in Table 3.

Table 2 describes a comparison between analytical model and FEA model. Furthermore, it points out how the introduction of the retainers decreases the maximum stress on one hand and, on the other hand, it moves the most stressed point close to the internal hook constraint point, that is, in the spring intrados, 10° from the internal hook.

Table 3 describes a comparison between FEA results and experimental results. The results reported in Table 3 were obtained by means of spring models with retainers. In this case, due to accessibility, strain gauges related to points 1 and 2 were positioned in spring extrados. The corresponding simulated values are reported in the same table.

Condition 1 of Table 3 is comparable with results in Table 2, considering that the stress in the intrados is higher than the extrados as absolute value: 1130 versus −930 MPa. Generally speaking, it resulted that the FEA calculated stresses are higher than experimental ones with an average difference about 10%.

Another experimental validation was performed by means of burst tests. In this case, the numerical estimation of the maximum speed, which leads to plastic strain was lower than the experimentally tested one.

**Figure 7.** Component *S-N* diagram.

Fatigue analysis

In Figure 7, the component experimental *S-N* diagram is reported, obtained from tests run in laboratory conducted using a durability test rig (Figure 8) on isolated components and $R = -1$. The run out points refer to springs which overcame 2 millions cycles, while blue points refer to the failure probability of 0.1%. The diagram was built by means of approximating the blue points with two linear functions until the fatigue strength $\sigma_{D-1} = 670$ MPa. The stress in the diagram is the stress obtained by means of strain gauge measurements.

Then, the fatigue analysis on the DMF spring was further developed by running two different sets of experiments.

In the first set, laboratory tests were performed on an instrumented vehicle. These run-up tests were done with the throttle pedal set to different percentages, in order to obtain the torque curves for several engine

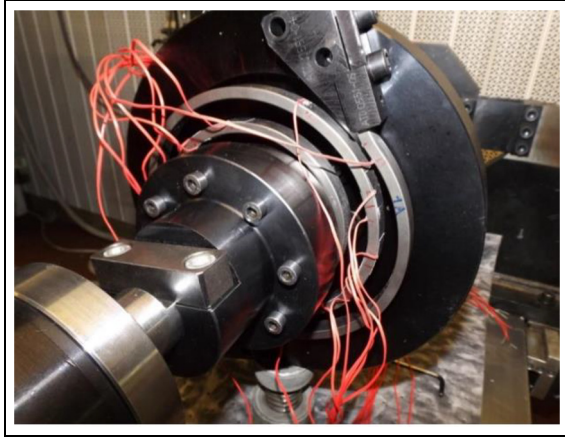


Figure 8. Component durability test rig.

load conditions. These tests aimed at relating driving configurations (time, throttle pedal position, and engine speed) with corresponding engine torque. These torque values were used as input data to FEM simulation to obtain the corresponding stresses in the critical spring points.

An example of results obtained from these tests is reported in Figure 9, which depicts the engine characteristic diagram related to five discrete engine load degrees adopted for building the considered duty cycle.

Every working condition in terms of rotational speed and torque has a related maximum principal stress on the DMF springs. In order to apply the fatigue approach with Rainflow counting and Palmgren-Miner damage computation, it is necessary to obtain a stress history.

To this aim, first of all the discrete values of torque related to each driving configuration were used as load-ing conditions for FEM simulations.

These simulations returned the corresponding stresses in the most loaded points of the spring in each driving condition and then the load case matrix was turned in a stress matrix which reports the max principal stress values.

In Table 4, as an example, the stress matrix is reported for the point indicated as 4 in Figure 5.

The most stressed part of the spring is located close to the inner hook. In Figure 10, the simulated stress at inner hook in -37 Nm and 6000 rpm conditions are reported as an example. The maximum principal stresses at this location can be calculated for the different mean and amplitude loading conditions to obtain the stress history of the most loaded point.

Once these two matrixes are defined for each driving configuration, the following step consists computing the time percentage with which the engine works in different discrete driving conditions. This is obtained from the experimental duty cycle.

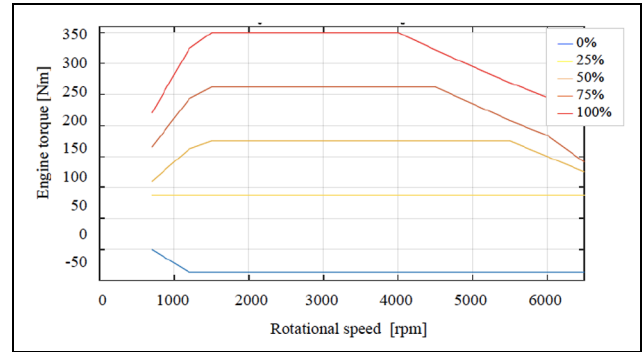


Figure 9. Engine characteristic with different engine loads (Dayco—all rights reserved). Curves are referred to different % of engine load.

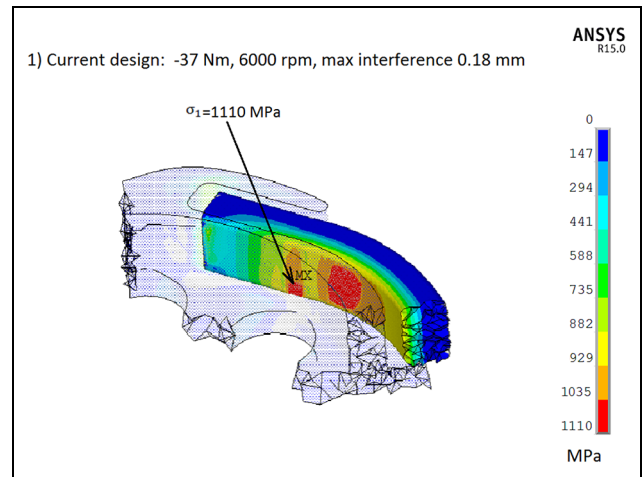


Figure 10. Simulated stress at inner hook.

To this aim, in the second test set, a real mission duty cycle was obtained by driving an instrumented vehicle on a defined path. Generally, a duty cycle includes many road types and corresponding driving configurations, to give a drive pattern representing standard vehicle life cycle. The single driving condition can work with different torque and rotational speed and durations, thus for every driving condition the corresponding load case matrix is required. The load case matrix represent discrete load cases, obtained in different driving conditions (city, highway, downhill, sport, etc.) related to the % time in each driving configuration, obtained by means of experimental acquisitions.

The present measured duty cycle consists of four sub-cycles, indicated in Figure 11: 30 acquisitions, of 52 km (80 min) each, were performed and repeated in an annular path. The sub-cycle distribution has been directly acquired throughout a smartphone app, during an experimental performance from the start to the

Table 4. Load stress matrix for node 4.

Principal stress (MPa)		Engine load (%)				
		0	25	50	75	100
Engine speed (rpm)	700	7	-227	-308	-308	-402
	1200	130	-218	-433	-607	-806
	1500	145	-209	-428	-606	-808
	2000	181	-189	-418	-601	-809
	2500	235	-157	-402	-594	-812
	3000	312	-110	-371	-581	-821
	3500	415	-37	-328	-555	-816
	4000	415	97	-247	-516	-801
	4500	634	290	-82	-423	-715
	5000	758	424	165	-105	-483
	5500	906	573	335	132	-56
	6000	1103	732	497	449	275
	6500	1277	907	676	676	521

Table 5. Load matrix for city sub-cycle.

Time (%)		Engine load (%)				
		0	25	50	75	100
Engine speed (rpm)	700	1.5	2.8	0.3	0.3	0.3
	1200	4.5	8.3	0.8	0.8	0.8
	1500	6	11	1	1	1
	2000	7.5	13.8	1.3	1.3	1.3
	2500	4.5	8.3	0.8	0.8	0.8
	3000	3	5.5	0.5	0.5	0.5
	3500	1.5	2.8	0.3	0.3	0.3
	4000	0.9	1.7	0.2	0.2	0.2
	4500	0.6	1.1	0.1	0.1	0.1
	5000	0	0	0	0	0
	5500	0	0	0	0	0
	6000	0	0	0	0	0
	6500	0	0	0	0	0

finish point. In Table 5, the load matrix related to city sub-cycle is reported as an example.

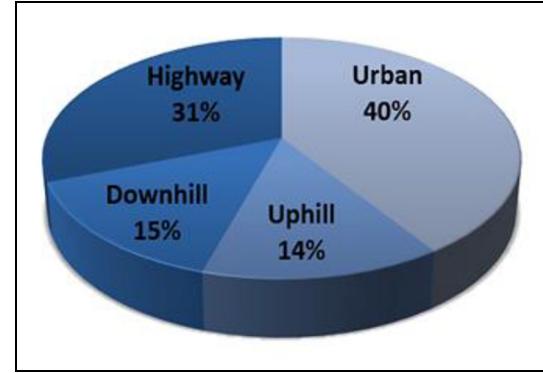
The experimental duty cycle takes into account of engine torsional vibrations, which are included in the test acquisitions, and it considers other aspects related to spring fatigue life as well as the material, heat and mechanical treatments, geometry, and shapes.

Each parameter presented for the single sub-cycle diagram is an average based on the, respectively, sub-cycles of 30 laps. These values are obtained computing first the average of each sub-cycle taking into account a single lap. Then, the final values are obtained through the average of all the same sub-cycle considering all the laps.

Every working condition in terms of rotational speed and torque has a related maximum principal stress.

The MATLAB script made by Dayco combines the engine speed with the engine load. The script examines value by value the throttle pedal signal (which is directly proportional to the engine load) and allocates the corresponding engine speed value in the array with which the engine load belongs. Each parameter obtained for the single sub-cycle diagram is an average based on the corresponding sub-cycles of 30 laps. Then, these driving conditions were combined in a random way to obtain the duty cycle stress history, by means of a dedicated MATLAB function, which returns an array with a random stress sequence. This sequence is suitable for the next step, that is, the fatigue approach by means of the Rainflow counting method and Palmgren-Miner rule implementation.

The software J-Rain by Jesmond Engineering carries out the Rainflow count. The output is a matrix with maximum and minimum stresses for all the counted cycles. Then, mean $\sigma_{m,i}$ and alternate $\sigma_{alt,i}$ stresses are calculated for each counted cycle and limit alternate

**Figure 11.** Sub-cycles in time (%).

stress $\sigma_{alt,i}$ is calculated per each cycle as follows²³ (equation (4))

$$\sigma_{alt,i} = \frac{\sigma_{alt,i}}{1 - \frac{\sigma_{m,i}}{UTS}} \quad (2)$$

where UTS is the spring material ultimate tensile strength (UTS).

If $\sigma_{alt,i}$ is higher than $\sigma_{alt,i}$, then the corresponding cycle is accounted as a damaging one and the corresponding damage is counted following the equations. Cycle follows equations (3) and (4) according to Palmgren-Miner

$$C_i = N_{ki} \sigma_{D-1}^{ki} \quad (3)$$

$$d_i = \frac{\sigma_{alt,i}^{ki}}{C_i} \quad (4)$$

Finally, the total damage D is the sum of all damages d_i . The load history of the spring is random and

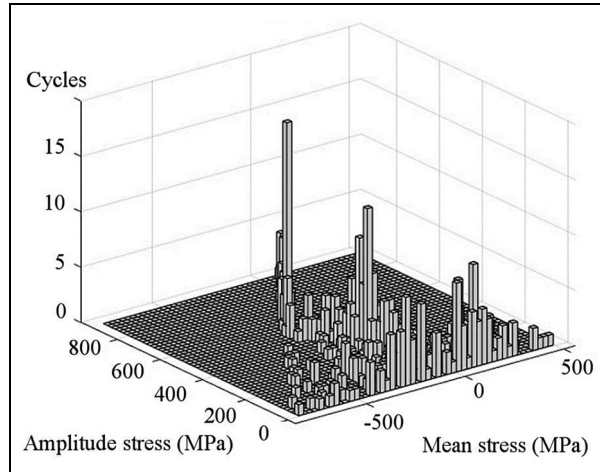


Figure 12. Histogram of experimental duty cycle.

then the damage critic value is 1. When the total damage, calculated according to equation (4), reaches the critical value, the spring is supposed to fail.

In addition, the single sub-cycles can be analyzed to evaluate which one is the worst.

Life estimation

Table 6 contains the results of the fatigue analyses for the worst three laps of the experimental duty cycle calculated in the inner hook, intrados.

Figure 12 depicts a histogram with the number of cycles corresponding to all the combination in terms of mean and amplitude stress. It results that there are several cycles with a very-high amplitude stress.

Tests with vehicle pointed out premature failures which do not match the fatigue life estimation (150,000 km in the worst case): four vehicle tests failed for 1000, 2258, 2587, and 25,000 km of vehicle route. The failure location is near the inner hook. All the other parts are in good status. The fracture surfaces denote wear and fatigue damages. In Figure 13, an example is reported. The examination of the inner spring holders reveals scars and marks, which

Table 6. Lifetime predictions for the worst laps of experimental duty cycle.

Lap number	Lifetime prediction (km)
1	153,035
22	186,039
13	241,915

associated with little burn signs, indicate that fretting could be present.

This means that damage and crack nucleation causes have to be found in fretting and in dynamic effects (which can lead to much higher stress than calculated ones). FEA analysis does not consider wear and fretting phenomena, thus underestimating maximum stress damage. This can be the cause of mismatch between experimental and simulated data. Furthermore, dynamic simulations show that for 350 N m and 4000–5000 rpm, stresses are amplified due to a bending resonance condition.

However, with the application of the measured duty cycle and considering the most stressed strain gauge, the fatigue analysis has a good response. Evaluating the damage of each 30 laps, the worst lap verifies the target that corresponds to 150,000 km. The computation is affected by many factors, as well as the driver, the weather, and traffic conditions, so there is a large scatter in the results, nevertheless it is possible with precaution consider the worst laps as a good result.

Conclusion

Spiral springs applied to DMF allow good performance in terms of filtering function, but due to design constraints, as well as installation space, production processes, stiffness requirement, maximum torque, and maximum speed, they cannot be dimensioned for infinite life.

FEA and experimental analysis reveals that the most stressed spring point is at the intrados of the inner hook, close to the fixation. The experimental

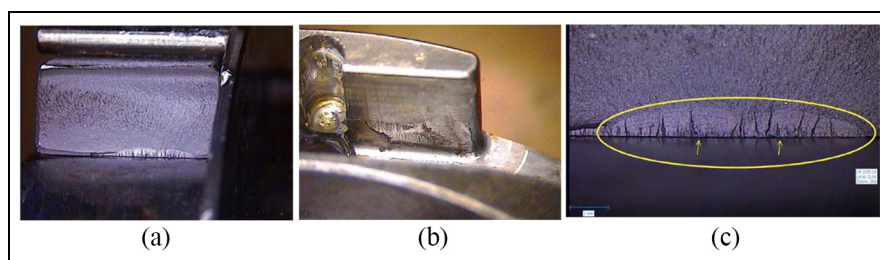


Figure 13. Failures of DMF springs: (a) fracture surface inside the spring holder, (b) detail of the inner spring holder, and (c) detail of the fracture surface.

characterization of the fatigue strength and the definition of the S - N diagram (stress–life), on isolated components, give the basic data for finite life fatigue computation.

An experimental duty cycle was acquired on vehicle and implemented in life estimation. It applies an actual stress history, but the computation is affected by many factors, resulting in a large results scatter, nevertheless it is possible to assume the worst laps for calculating loading history and obtaining a reliable simulation result.

Tests on vehicle confirm that the failures take place where the finite element simulation calculated the higher stresses and that the crack starts from the inner spring hook side. Vehicle tests highlight premature spiral springs' breakages for shorter life than estimated. The examination of the fracture leads to the conclusion that the problem is related to fretting happening at the fixation. This phenomenon was not considered in life estimation models.

In laboratory bench testing of isolated components, life estimation was verified, while when duty cycles were simulated, failures occurred for life much shorter than estimations. This implies that for these components, the fatigue life is strongly influenced by loading history, while the Palmgren-Miner model neglects or underestimates it.

The same happens for friction and wear, which are not taken into account in FEA and appear to be the main crack initiation causes. Since friction is part of the device's operation, it is not possible to reduce it or consider it negligible. However, the combination of two methods, Rainflow and Palmgren-Miner life estimation showed itself inadequate, so it will be necessary introduce corrections or consider different model applications.

The presented results can be relevant for flywheel design optimization. Furthermore, the fatigue design procedure can be applied for other components. Aim of the research was, in fact, to define a prediction model able to describe the phenomenological aspects, to minimize the experimental testing. The mismatch between the experimental and prediction results encourage to deeper investigate the problem and evaluate the influence of fretting and dynamic contribution to system damage in order to increase the reliability of the model.


Declaration of conflicting interests

The author(s) declared no potential conflicts of interest with respect to the research, authorship, and/or publication of this article.

Funding

The author(s) received no financial support for the research, authorship, and/or publication of this article.

ORCID iD

Raffaella Sesana  <https://orcid.org/0000-0002-2810-6291>

References

- Schaper U, Sawodny O, Mahl T, et al. Modeling and torque estimation of an automotive dual mass flywheel. In: *Proceedings of the American control conference*, St. Louis, MO, 10–12 June 2009, pp.1207–121. New York: IEEE.
- Mahl T and Sawodny O. Modelling of an automotive dual mass flywheel. In: *Proceedings of the IFAC symposium on mechatronic systems*, Cambridge, MA, 13–15 September 2010, pp. 517–523. New York: Elsevier.
- Theodossiades S, Gnanakumarr M, Rahnejat H, et al. Effect of a dual-mass flywheel on the impact-induced noise in vehicular powertrain systems. *Proc IMechE, Part D: J Automobile Engineering* 2006; 220: 747–761.
- Khochare T. Advance development in dual mass flywheel. *Int J Recent Innov Trends Comput Commun* 2015; 3: 5401–5408.
- Baran P and Grega R. Comparison of dynamic properties of dual mass flywheel. *Diagnostyka* 2015; 16: 29–33.
- Shelke RS and Dighole DG. A review paper on dual mass flywheel system. *Int J Sci Eng Technol Res* 2016; 5: 326–331.
- Chen L, Zeng R and Jiang Z. Nonlinear dynamical model of an automotive dual mass flywheel. *Adv Mech Eng* 2015; 7: 1–11.
- Lokhande S, Sonawane DP and Londhe BC. Review on design and manufacturing of dual mass flywheel. *Int J Innov Res Sci Eng* 2016; 2: 255–268.
- Yan Z, Zhou K and Liao C. Reliability analysis of the dual mass flywheel damping flange based on workbench. In: *Proceedings of the 3rd international conference on materials engineering, manufacturing technology and control (ICMEMTC 2016)*, Taiyuan, China, 27–28 February 2016, pp.1362–1368. Atlantis Press.
- Chen D, Ma Y, Sun W, et al. Research of design and vibration reduction of dual mass flywheel with arc helix spring. In: *Proceedings of the 2011 international conference on electronic & mechanical engineering and information technology*, Harbin, China, 18–20 January 2011, pp.2706–2709. New York: IEEE.
- Kang T-S, Kauh SK and Ha K-P. Development of the displacement measuring system for a dual mass flywheel in a vehicle. *Proc IMechE, Part D: J Automobile Engineering* 2009; 223: 1273–1281.
- Cariccia G, Giansetto G, Montani A, et al. *Dual mass flywheel*. US 2014/0338493 A1 Patent, 2014.
- Cariccia G, Giansetto G, Montani A, et al. *Improved dual mass flywheel*. WO/2013/057728 A2 Patent, 2013.
- Giansetto G, Montani A, Cariccia G, et al. *Spiral spring dual mass flywheel having a parallel configuration*. WO 2013/139983 A1 Patent, 2013.
- Barradas Berglind JJ and Wisniewski R. Fatigue estimation methods comparison for wind turbine control. *IET Control Theory A* 2015; 9: 1042–1050.
- Baek SH, Cho SS and Joo WS. Fatigue life prediction based on the Rainflow cycle counting method for the end

- beam of a freight car bogie. *Int J Automot Technol* 2008; 9: 95–101.
17. Fatemi A and Yang L. Cumulative fatigue damage and life prediction theories: a survey of the state of the art for homogeneous materials. *Int J Fatigue* 1998; 20: 9–34.
 18. ASTM E1049-85:2017. Standard practices for cycle counting in fatigue analysis.
 19. Roshanfar M and Salimi MS. Comparing of methods of cycle calculating and counting to the rain flow method. *Exten J Appl Sci* 2015; 3: 291–296.
 20. Tovo R. Cycle distribution and fatigue damage under broad-band random loading. *Int J Fatigue* 2002; 24: 1137–1147.
 21. Ligaj B. An analysis of the influence of cycle counting methods on fatigue life calculations of steel. *Sci Prob Mach Oper Main* 2011; 4: 25–44.
 22. Downing S and Socie D. Simple Rainflow counting algorithms. *Int J Fatigue* 1982; 4: 31–40.
 23. Goodman J. *Mechanics Applied to Engineering*, Longman, Green & Company, London, 1899.